ChemCatChem

Research Article
doi.org/10.1002/cctc.202200300

Chemistry Europe
European Chemical Societies Publishing

www.chemcatchem.org

Special Collection

Sr Surface Enrichment in Solid Oxide Cells – Approaching the Limits of EDX Analysis by Multivariate Statistical Analysis and Simulations

Hanna Türk,[a, b] Thomas Götsch,[a] Franz-Philipp Schmidt,[a] Adnan Hammud,[a] Danail Ivanov,[a] L. G. J. (Bert) de Haart,[c] Izaak C. Vinke,[c] Rüdiger-A. Eichel,[c, d] Robert Schlögl,[a, e] Karsten Reuter,[a] Axel Knop-Gericke,[a, e] Thomas Lunkenbein,*[a] and Christoph Scheurer*[a]

In solid oxide cells, Sr segregation has been correlated with degradation. Yet, the atomistic mechanism remains unknown. Here we begin to localize the origin of Sr surface nucleation by combining force field based simulations, energy dispersive X-ray spectroscopy (EDX), and multi-variate statistical analysis. We find increased ion mobility in the complexion between yttria-stabilized zirconia and strontium-doped lanthanum manganite. Furthermore, we developed a robust and automated routine to detect localized nucleation seeds of Sr at the complexion surface. This hints at a mechanism originating at the complexion and requires in-depth studies at the atomistic level, where the developed routine can be beneficial for analyzing large hyperspectral EDX datasets.

Introduction

Solid oxide cells (SOCs), including solid oxide fuel cells (SOFCs) and solid oxide electrolysis cells (SOECs) are becoming increasingly important due to their relatively high energy conversion efficiencies of up to 85 %.[1,2] This makes solid oxide cells a valuable element to complement the modern energy infrastructure by providing chemical storage capacities for excess energy that temporarily arises due to the intermittent nature of renewable energy sources such as wind or solar power.[3]

The wide-spread adoption of these cells is currently hindered primarily by a fast degradation of the anode in electrolysis mode. This electrode is responsible for the oxygen evolution reaction (OER).[4,5] It is believed that oxygen evolution occurs at the triple phase boundary (TPB) where the oxygen-ion-conducting electrolyte (usually yttria-stabilized zirconia, YSZ), the electron-conducting electrode (often a perovskite, here lanthanum strontium manganite, LSM) and the gas phase meet.[6–8] While the location of this point is defined by indispensable properties to allow the OER to proceed, e.g. having sufficiently high oxygen ion and electron conductivity, the point itself, however, remains an elusive concept that has never been directly observed so far. Elucidating the structure of the TPB and its thermodynamic stability is crucial to identify the relevant aging process within the plethora of proposed deactivation mechanisms.[9] Besides poisoning[5] and electrode delamination caused by internal oxygen partial pressure[4,10–12] or YSZ electroreduction,[13] cation (Sr and Mn) migration is believed to play a key role in electrode deactivation. It is responsible for interfacial reactions,[14–18] nanocluster formation,[19] structural damages,[20] loss of electronic conductivity in LSM[21–24] and active site blockage by the respective oxides as well as subsequent surface reactions of the cations with volatile species.[17,22,23,25–27]

Already in the early stages of SOFC development at FZ Jülich,[28,29] an A-site deficient LSM composition was selected, because in combination with the YSZ electrolyte this composition is less susceptible to the undesired formation of a $La_2Zr_2O_7$ interlayer during sintering of the LSM electrode layer at

[a] H. Türk, Dr. T. Götsch, Dr. F.-P. Schmidt, A. Hammud, D. Ivanov, Prof. R. Schlögl, Prof. K. Reuter, Dr. A. Knop-Gericke, Dr. T. Lunkenbein, Dr. C. Scheurer
Fritz-Haber-Institut der Max-Planck-Gesellschaft
Faradayweg 4–6, 14195 Berlin (Germany)
E-mail: lunkenbein@fhi.mpg.de
scheurer@fhi.mpg.de
[b] H. Türk
Chair for Theoretical Chemistry and Catalysis Research Center
Department of Chemistry
Technische Universität München
Lichtenbergstraße 4, 85748 Garching (Germany)
[c] Dr. L. G. J. (Bert) de Haart, Dr. I. C. Vinke, Prof. R.-A. Eichel
Forschungszentrum Jülich GmbH
Institute of Energy and Climate Research
Fundamental Electrochemistry (IEK-9)
Wilhelm-Johnen-Straße, 52428 Jülich (Germany)
[d] Prof. R.-A. Eichel
RWTH Aachen University
Institute of Physical Chemistry
Landoltweg 2, 52074 Aachen (Germany)
[e] Prof. R. Schlögl, Dr. A. Knop-Gericke
Max Planck Institute for Chemical Energy Conversion
Department of Heterogeneous Reactions
Stiftstraße 34–36, 45470 Mülheim an der Ruhr (Germany)

Supporting information for this article is available on the WWW under https://doi.org/10.1002/cctc.202200300

Special Collection

This publication is part of a joint Special Collection with ChemElectroChem on "Catalysts and Reactors under Dynamic Conditions for Energy Storage and Conversion (DynaKat)". Please check our homepage for more articles in the collection.

elevated temperatures (1250 to 1350 °C).[30–32] Further segregation mitigation strategies include nanoparticle infiltration[33] and anode[34] and microstructure[35] design to suppress high oxygen partial pressure[36] and anodic polarization,[20] which have been proposed to drive this phenomenon. Even though these strategies have shown promising results, cation segregation, especially of Sr, continues to impact cell performance, as the absence of fundamental understanding on the atomistic level prevents its systematic control.[37,38]

Previously,[39,40] we have shown that a so-called complexion is formed between the typical components of the cell, i.e. the YSZ electrolyte and the LSM anode. In brief, a complexion is a thermodynamically stable intergranular layer of self-limited width that is only stable in between two bulk phases.[41,42] Complexions have already been found in a variety of different functional solids.[43–48] Such a complexion can exhibit properties different from their neighboring phases. For SOCs, many of these properties are not yet identified or understood. For instance, it may be a mixed ionic and electronic conductor (MIEC),[39] which would ideally increase the size of the location of oxygen evolution from a 1-dimensional (1D) line to a 2D complexion/gas area containing the active sites if it extends unperturbed to the surface. In reality, however, the surface structure and composition of oxides differs from the underlying bulk.[49,50]

In the present study, we aim at assessing the composition of the surface termination of the complexion by combining simulation and experiment. Therefore, the manuscript is hierarchically structured and we first take a closer look at the chemical properties inside the complexion by evaluating molecular dynamics simulations to understand spatially resolved ion mobilities. We found a variation of the oxygen ion diffusion within the complexion compared to the neighboring bulk phases. Second, we investigated the cation mobility in this partially amorphous layer and predict a stable surface composition of the complexion by Monte Carlo (MC) simulations. The evolution of the elemental distribution towards the complexion surface was investigated emphasizing the role of strontium cations, which were previously found to be almost absent from the unperturbed complexion. It was found that the elemental profile associated with Sr across the complexion was shifted significantly compared to all other elements.[39] Experimentally, we employ energy-dispersive X-ray (EDX) spectrum images in a (scanning) transmission electron microscope ((S)TEM) for aged samples (150 h at 1073 K). In addition, complementary synchrotron-based X-ray photoelectron spectroscopy (XPS) measurements were performed for the aged and the pristine samples (1423 K for 1 h).

The detection of small, local (i.e. sub-nanometer) variations in the elemental distribution represents a key challenge when it comes to low concentration elements. STEM-based EDX is a well-suited technique to study such local variations due to its high spatial resolution given by the focused electron probe. However, the limited collection efficiency of the generated X-rays leads to high noise levels hindering a clear interpretation of potential changes in the elemental distribution. This can become problematic if the respective elemental concentrations drops below 5 at%, which holds also for the Sr content within the LSM used in this study ($(La_{0.8}Sr_{0.2})_{0.95}MnO_{3-\delta}$). Within the complexion,[39] the Sr content is further reduced to below 2 at%. Although there has been a huge progress within the last decade to increase the X-ray detection efficiencies, the measurement of minute variations of a small amount of an element at the sub-nm scale remains still challenging.

To overcome this dilemma we here apply a novel approach that consists of four steps: (1) We have optimized the acquisition procedure to obtain the best trade-off between high signal and low/no beam damage. (2) We performed a post-acquisition sample drift correction and (3) utilized multivariate statistical analysis (MSA)[51–56] by applying non-negative matrix factorization (NMF).[57,58] (4) Welch's t-testing was finally employed to evaluate an increase or decrease of the Sr content along the complexion towards a potential TPB.

In general, MSA is used to find inference of more than two variables in empirical datasets.[59,60] Besides many other fields, it has successfully been applied in medicine[61,62] and biology.[63] In electron microscopy, the main application of dimensionality reduction by MSA is denoising of spectra, often by principal component analysis (PCA).[64,65] However, these methods are increasingly also used to decompose hyperspectral stacks obtained from spectrum imaging in order to extract different, also overlapping, components from EDX or electron energy-loss (EEL) spectra. This can be used to map different phases that are non-trivial to distinguish spectroscopically.[66–68]

The Sr variations are additionally investigated by means of XPS, which enables the comparison of surface to sub-surface ("bulk") Sr content. It further allows the analysis of its chemical nature. However, being a spatially integrative technique with much worse lateral resolution compared to EDX and Sr segregation has also been shown for pure perovskites,[69] the sample was carefully polished in order to expose as many complexion/vacuum interfaces as possible to the X-ray beam.

Results and Discussion

Simulation

Ion diffusion

For OER, oxygen ion and electronic conductivity around the active phase is essential as it determines the availability of O^{2-} at the recombination zone. In addition, the concept of TPB may be supported by the presence of a complexion, albeit by a possible higher dimensionality. Complexions can have different properties compared to their confining bulk phases, e.g. partial amorphization and compositional gradients.[46] We focus here on the ion transport properties within the complexion which has not been investigated until now.

We performed molecular dynamics (MD) simulations to assess the ion mobility along the complexion. Figure 1 shows the extracted diffusion coefficients of all ionic species for several relevant temperatures. At each temperature, the total ion mobility is significantly increased within the complexion as

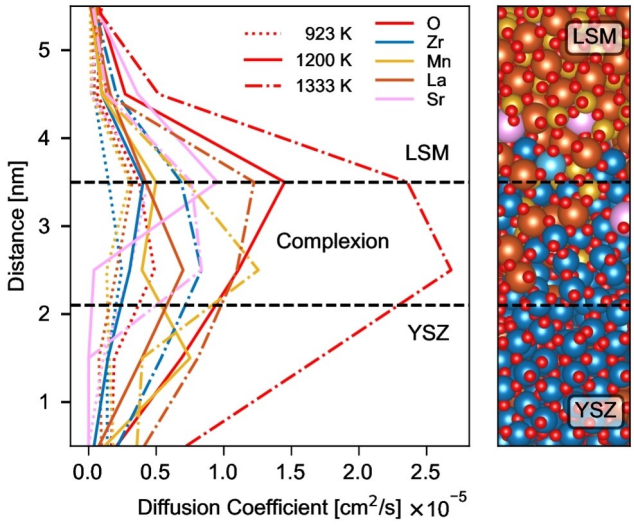

Figure 1. (left) Diffusion coefficients of different ions across the complexion at different temperatures (dotted lines: 923 K, solid: 1200 K and dash dotted: 1333 K). The dashed black lines enclose the complexion. (right) Exemplary excerpt of one complexion with its confining bulk phases. The color code of the elements is the same as for the diffusion, Y is highlighted in light blue.

compared to the bulk phases. This effect is most pronounced for the oxygen anions, suggesting a more than three-times increase of the ion mobility as compared to the adjacent YSZ bulk phase. Such an enhancement of oxygen ion conductivity has been reported before for LSM grain boundaries,[70] which was attributed to the high density of oxygen vacancies in this area. In our case the observed high oxygen ion mobility may stem from a reduced density as a consequence of the partial amorphization of the complexion. According to the simulations, the oxygen density in the complexion yields only 83.1% and 83.3% of the one of LSM and YSZ, and the total mass density is reduced to 78.4% of the LSM bulk and 98.6% of the YSZ (compare Table S1 in the SI for density values). Note that the bulk density values are, due to simulation cell size limitations, extracted only a few nanometers away from the complexion and thus can still be influenced by it. This reduced density in the complexion could open space for oxygen diffusion and facilitate ion movement. The enhancement of oxygen ion mobility might be considered an intrinsic property of grain boundaries and complexions in ion conducting host materials as long as free oxygen sites are available. The high oxygen mobility within the complexion may be important for the function of the SOEC to maintain a steady surface oxygen supply and to regulate the oxidation states of the surface metals.

Remarkably, not only the oxygen ion mobility is considerably enhanced in the area of the complexion, but also the cations become fairly mobile within the complexion. However, a high cation mobility could enhance segregation and thus lead to irreversible restructuring effects. This poses the question whether the elemental composition within the complexion as established during the sintering process is stable during the prevailing time of the operation, in particular in the vicinity of the active surface. In reality the LSM/YSZ interface is multiplied in a porous layer of approximately 25 μm thickness, which exposes several active areas to the gaseous environment.[39] In order to obtain a realistic thermodynamic equilibrium model from infinite simulation slabs, covering not only a complexion between the two adjacent oxide phases but also the exposed active surface, we cut a rectangular hole through this arrangement (see SI Figure S1). This may facilitate the exploration of compositional restructuring, which could be a reason for the fast anode degradation.

Complexion surface termination

To assess this question, we simulated sintering and thermal aging by an MC approach for an ensemble of model cells containing surfaces exposed to vacuum that cut across the complexion to study the evolution of the surface composition of the complexion at an atomistic level. The top and side views of the complexion/vacuum interface for one exemplary cell after convergence of the MC simulation are shown in Figure 2a and b. The simulations show that the Sr ions (pink) are accumulating on this surface in the vicinity of the complexion in the form of an oxide.

To quantify this effect, Figure 2c features the ensemble averaged elemental profiles along the complexion up to the vacuum interface. While oxygen and zirconium do not show a notable gradient from the complexion bulk towards the surface, Mn and Sr seem to significantly supplant La within the nanometer, which is closest to the surface. In comparison to Zr and O, this effect is the strongest for Sr, where the elemental profile is even shifted slightly towards the surface, whereas for La and Mn the profiles' points of inflection are shifted towards the bulk region of the complexion. While the general phenomenon of Mn[71–73] and Sr[7,24–26,73–77] surface segregation in LSM has been reported for various conditions and doping concentrations, Sr segregation has even been linked to cell performance.[22,23,27,38] Note that this simulation, performed without any polarization and neglecting the oxygen partial pressure, yields the same results as experiments under various experimental conditions. Hence, cation segregation seems to lead to a broad thermodynamic minimum, whose reach can only be suppressed sufficiently if the mechanism leading there is understood. The highly localized deposition on the complexion/vacuum interface, in combination with the observed high cation mobilities in this area, hints towards a segregation mechanism via the complexion.

Thus, we propose a complexion-mediated cation segregation pathway, which is illustrated for Sr in Figure 2d. Instead of migrating via the LSM bulk to the surface, where cation diffusion is severely limited,[24] cations close to the grain boundary diffuse into the complexion, which features a significantly enhanced ion mobility. The enhanced diffusion in the complexion leads to a faster thermodynamic equilibration, which, according to our simulations, includes Sr and Mn oxide formation on the complexion surface.

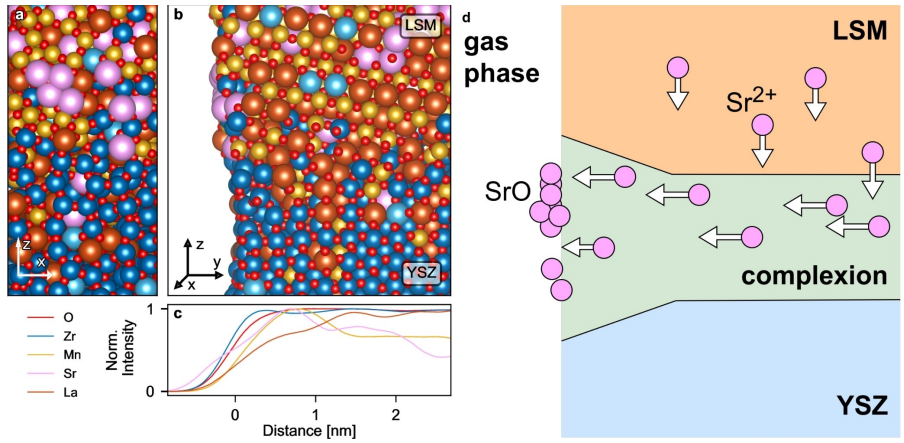

Figure 2. (a) Top view of one simulated cell showing the complexion/vacuum interface. (b) Cut through the surface shown in (a) to show complexion evolution to the surface. (c) The normalized intensity of the elemental profiles from the vacuum along the complexion obtained by overlaying the atoms ±7 Å from complexion center with 3D Gaussian functions and projection onto the y dimension. (d) Proposed cation segregation pathway to the complexion surface, illustratively shown for Sr.

In addition to the often contemplated effect of reduced electronic conductivity in LSM due to Sr bleeding, this surface oxide formation might actually result in physical blockage of active sites.[38] It may thus render Sr segregation into a potentially active zone, i.e. the surface of the complexion, a plausible source for degradation. The driving force behind this mechanism might be electrostatic and elastic interactions of the cations in the complexion, which are believed to cause Sr segregation in pure LSM,[38] and agree with our findings that Sr is almost absent within the complexion.[39] However, further studies are required to fully elucidate the mechanistic details of this pathway.

Experiments

Cation mobility

In order to validate the simulation results we analyzed the aged sample (150 h, heated up to 1173 K) by STEM-EDX. We first investigate the cation diffusion along the grain boundaries. Figure 3 shows part of the LSM/YSZ mixed electrode close to the interface of the YSZ electrolyte (for details on the cell structure see Ref. [39]). The phase separation between the LSM and YSZ phase is depicted in Figure 3a by elemental maps. Together with a bright field (BF) TEM image (left), the elemental distribution is revealed by a combined Zr/La EDX map (blue/red) and single EDX maps of Mn (yellow), La (red) and Sr (pink). As predicted by the simulations discussed above, Mn and La exhibit increased mobility trough the complexion into YSZ and its grain boundary, which is highlighted in Figure 3b. At the grain boundaries between different YSZ grains, the Mn and La signals could be detected as shown by an enhanced signal, indicating cation diffusion along these grain boundaries (see also yellow and red arrow, respectively). For Sr, in contrast, we could not detect any signal, above the noise level, outside the LSM grains. Note, that the seemingly low Sr content in Figure 3b can not be attributed to a significant spectral Sr feature applying standard analysis routines. These findings on the diffusion or lack thereof of La, Mn, and Sr cations along the grain boundaries are further corroborated by Figure S3 in the Supporting Information. However, as found by simulations, mobility for Sr is also to be expected. Therefore, two questions arise: whether this negative finding is merely due to limitations in the data analysis and whether, it is possible to detect the predicted Sr diffusion and enhancement at the complexion/vacuum interface. Note, that the Sr content is nominally only 4 at% in the LSM phase and potentially much less outside the LSM grain.

Drift correction

To answer the question which emerges from the simulation experimentally is a rather complex challenge, as size of the simulated strontium oxide nucleation seed is rather on the Ångström than nanometer scale. Investigating such small variations of elemental concentration changes requires an analysis close to the microscopic resolution and detection limit and is, therefore, extremely challenging. On top, appropriate sample preparation to uncover potential complexion/vacuum interfaces for TEM investigations introduces an additional degree of complexity.

The small width of the complexion paired with the even smaller size of its interface with the gas phase evoke the need to assess minor changes in the concentration of individual elements with very high spatial resolution. Only this would enable us to prospectively track the whole surface oxide formation process from the beginning. This would also allow the investigation of its formation mechanism in full detail, which is necessary for its direct linkage to cell performance.

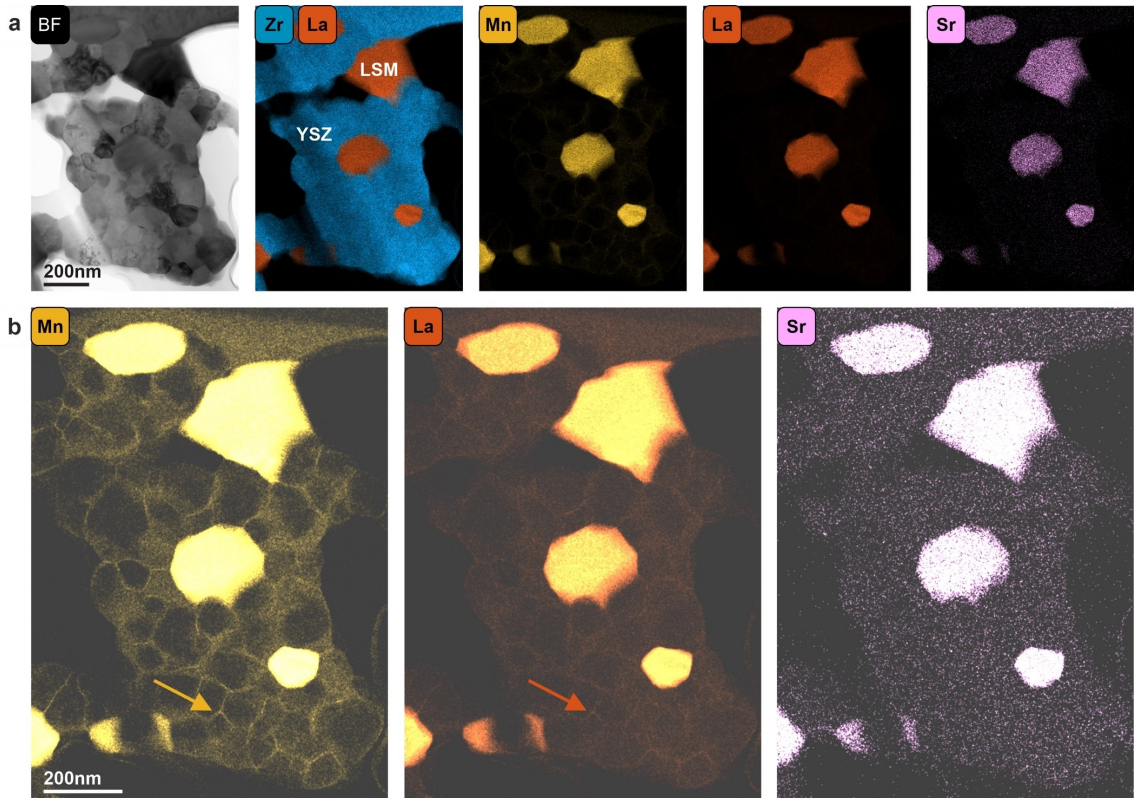

Figure 3. Cation mobility. (a) Bright field image (BF) of a mixed LSM/YSZ electrode and EDX elemental maps of zirconium and lanthanum (Zr/La), manganese (Mn), lanthanum (La) and strontium (Sr) of the corresponding region shown in BF. (b) Contrast- and brightness-adjusted maps of Mn, La and Sr highlight enhanced signal at the grain boundaries between different YSZ grains for Mn (yellow arrow) and less pronounced for La (red arrow). Sr is only resolved within the LSM grains, the low and homogeneous signal over the YSZ grains is attributed to residual background and noise contribution due the low Sr content.

To overcome the aforementioned issues, we developed a routine that is based on post-acquisition drift correction, component analysis and statistical analysis. The developed routine is demonstrated in the following. For details on the sample preparation and the optimized acquisition procedure for optimized signal detection to avoid e-beam induced artifacts which would limit any unambiguous interpretation, we refer to the Methods section.

In Figure 4a, BF images from different points in time during the acquisition of an EDX spectrum image close to the complexion/vacuum interface are displayed. Compared to the first frame, the additional images of this series exhibit significant drifts of several nanometers despite using the online drift correction of the acquisition software. Since this residual drift is much larger than the localization of the desired information, i.e. the strontium oxide accumulation, the spectrum images can hardly be used without further processing as the spectral information is blurred in an analog way. The top-left panel in Figure 4b shows the resulting image when summing up all BF images from all 175 frames in the EDX hyperspectral cube. Compared to the single snapshots, it appears very smoothed while well defined contrast changes are absent. This is further illustrated in Figure S6, where the effect is simulated on a 2D Gaussian with a full-width at half maximum of 1 nm and is shown to lead to strong delocalization and distortion.

Figure 4b also shows the results of different drift detection algorithms. Cross-correlation (top right), a standard technique used for such tasks, results in a minute improvement especially in the horizontal direction. However, it does not lead to significant improvements, even though there are sharp and significant contrast changes in the image. Thus, we employed a different approach in which 100 templates (a combination of manually and randomly placed ones, refer to Figure S4) are matched every frame, for each of the three image types that are acquired, i.e. BF, dark field (DF) and high-angle annular dark field (HAADF), resulting in 300 template matches each frame. This creates a much sharper image, which can be further improved if the image shift is not determined from all template matching results, but if an outlier check is first performed using the RANSAC algorithm.[78] This creates a summed image that is comparable to the single frames. Figure S7 highlights the effect of the RANSAC outlier removal: from the multitude of template match results (in gray), only the orange points are considered inliers. The drift detected by applying a Euclidean transform model to the RANSAC inliers follows the orange points closely (see the blue curve), whereas the one from all templates (green) deviates strongly, especially at high time values in x (horizontal direction) and already before that in y (vertical direction).

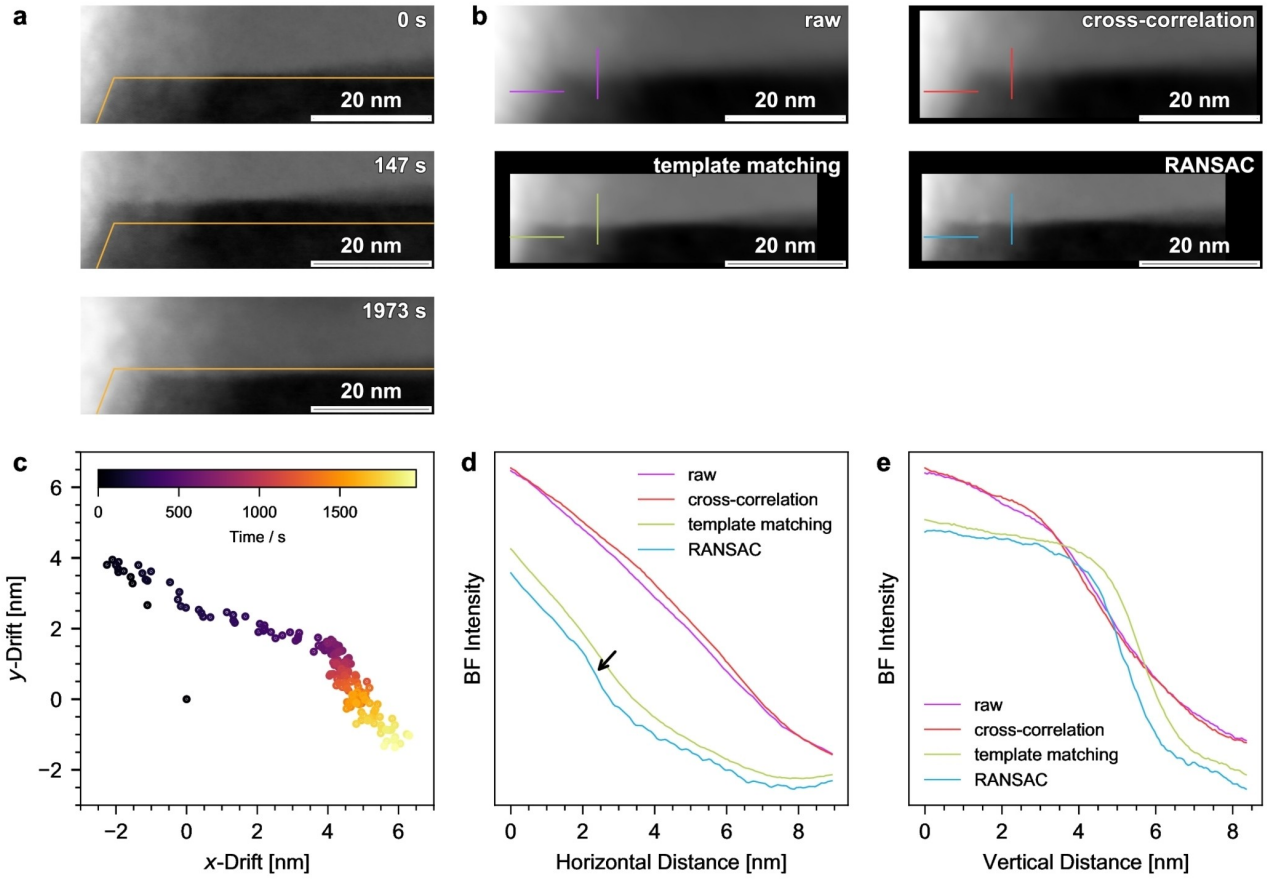

Figure 4. Post-acquisition drift correction. (a) Selected BF snapshots from different times during the spectrum image acquisition still show considerable drift with respect to the first frame at 0 s. The orange lines serve as guides to the eye to enhance the visibility of the drift still present in the raw data. (b) Comparison of the summed BF images without further correction ('raw') and after different post-acquisition drift correction algorithms. Image regions not present in every frame are masked, effectively cropping the available field of view. (c) The residual sample motion after acquisition, as measured using the RANSAC algorithm. In (d) and (e), intensity profiles along the lines indicated in b) are plotted. Neither the online drift detection ('raw'), nor cross-correlation yield adequate results and lead to very blurred contrast changes. RANSAC generates the sharpest steps and is the only technique to resolve the small step just above 2 nm in d) (see the arrow).

The temporal drift evolution from RANSAC in Figure 4c reveals that there is a fast sample motion in the beginning toward the top-left, which is in line with the images in Figure 4a, and then the sample drifts towards the lower right rather linearly, with a slight kink in the position distribution between 500 s and 1000 s. The sample drift thus spans a distance of around 8 nm in *x* and 5 nm in *y* direction, which is insufficient for detecting local information at the nanometer scale, let alone in the range of a few Ångström.

Figure S8 also shows the time-dependent drifts obtained from all methods. While RANSAC and template matching have similar trends, cross-correlation appears to be insufficient for the present images, explaining the blurred image. It should be noted that the corrected images are cropped because only pixels that are contained in every shift-corrected frame can contribute to the final image. Thus, the field-of-view is restricted. However, this is compensated by a gain in spatial resolution. This improvement can also be seen in Figure 4d and Figure 4e. In these figures, line profiles of the BF image in horizontal and vertical direction are plotted for the different drift correction types. As discussed before, cross-correlation only leads to a negligible improvement over the raw data as output from the microscope software. However, the vertical step is significantly sharper for both template-matching-based procedures, with RANSAC leading to the sharpest contrast change. Furthermore, in the horizontal profile, RANSAC is the only drift correction method that resolves the small step at around 2 nm, as indicated by the arrow in Figure 4d.

Component Analysis

The EDX data was analyzed and decomposed into individual elemental maps using two alternative, but complementary routes: (a) by standard evaluation tools and (b) by a standalone Non-Negative Matrix Factorization (NMF), which would enable automated analysis and add superior spatial resolution due to the possibility to apply additional drift correction and denois-

ing, i.e. less binning. Automated analysis is important in order to achieve a high throughput analysis, which would allow for a statistical evaluation of the sample at high spatial resolution and the tracking of nanostructural inhomogeneities at the complexion/vacuum interface. Spatial resolution is required as in the case of SOCs the Sr enrichment is an atomic scale phenomenon located at a small fraction of the sample. Results from the standard procedure are shown in Figure S9 and used as a reference for the NMF analysis. The results of the NMF analysis are shown in Figure 5. Additionally, the drift-corrected HAADF- and BF-STEM images are presented for comparison in the same figure. Complete results of the NMF are given in the SI Figures S10 and S11, as well as an analysis of the Sr signal in YSZ due to the overlap of Sr, Y and Zr spectral peaks in Figure S12.

While both methods are able to separate the EDX signal into the elemental maps, the drift corrected NMF yields sharper edges and higher contrast of intensities in comparison to the standard procedure. This allows for an improved quantitative analysis of the respective element distributions in the sample, even for the doping elements Sr and Y, which have comparably low concentration (approximately 3.8 at% in LSM and 5.1 at% in YSZ).

Comparing the elemental maps from both methods (Figure 5 and Figure S9), a prominent feature is the concentration edge in the oxygen map at the transition of YSZ to LSM obtained by both techniques. When taking a closer look at the oxygen density in the individual bulk materials, LSM is expected to have 86.8% of the oxygen number density of YSZ as calculated from experimental lattice parameters.[39] While the standard evaluation procedure yields a ratio of approximately 81%, the drift-corrected NMF data is able to capture this difference as well, yielding a ratio of 91% of the mean oxygen concentrations between LSM and YSZ (see Figure S13 in the SI for details). As opposed to the maps of the drift-corrected NMF analysis the elemental maps of the standard evaluation procedure appear more blurred at the interfaces. Overall this analysis shows that automated routines, such as drift corrected NMFs, can be used to efficiently analyze large EDX data stacks and perform high-throughput analysis in to order to understand local compositional variations of SOCs.

Statistical analysis

In order to resolve minute concentration differences of dopant species, such as Sr, with high spatial resolution, we perform Welch tests, i.e. statistical tests which are able to distinguish unequal mean values of sample distributions.[79] To demonstrate their performance, the tests were first applied to the bulk signal of the Sr elemental map. Figure 6a shows the complete relative spectral contribution of the Sr intensity map obtained by the drift-corrected NMF. The dashed black line marks the area in which the sample was found to possess a constant thickness. To the left, the sample features a wedge-like shape, becoming progressively thinner (compare SI Figure S14). Colored rectangles mark the positions of sections shown in the other subplots. For the first set of tests, the Sr map was divided into 25 equally sized areas, shown as blue rectangles in Figure 6b. The Sr concentration in each of those areas was compared to the same central Sr bulk area, marked by a dashed red boundary. Note that, as a consequence, the red-marked area is also compared to itself. A close-up of this reference area is shown in Figure 6c.

We performed two-sided Welch t-tests, meaning that the alternative hypothesis constitutes an either smaller or higher mean concentration in the respective areas of comparison. In order to conduct a Welch test comparing two areas, these areas are each sub-divided into 30 smaller regions. Each of the smaller sub-regions is 19.5 Å^2 in size, making the total compared areas 5.85 nm^2. The values within each sub-region are aggregated. From the resulting 30 cumulative intensity values, 15 were selected randomly (with replacement) and used in the test. One realization of the selected sub-regions within the compared areas resulting from this stochastic sampling process is exemplarily shown in Figure 6d for one of the blue areas and the reference area. The binning of the smaller sub-

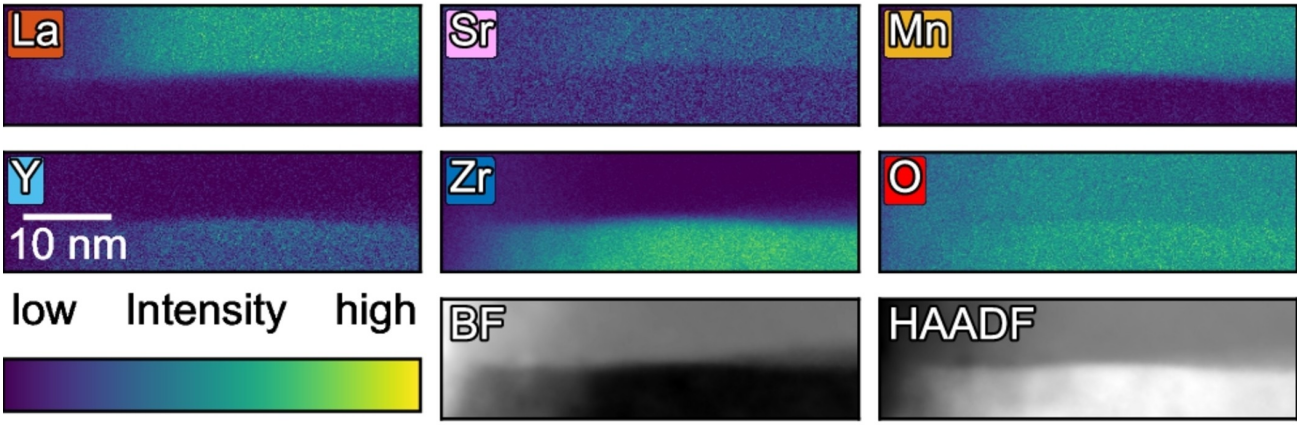

Figure 5. NMF decomposition of the EDX raw data after application of the drift correction. All elemental maps are binned (3×2 pixel bins). The binning was applied after the drift-correction and before conducting the NMF.

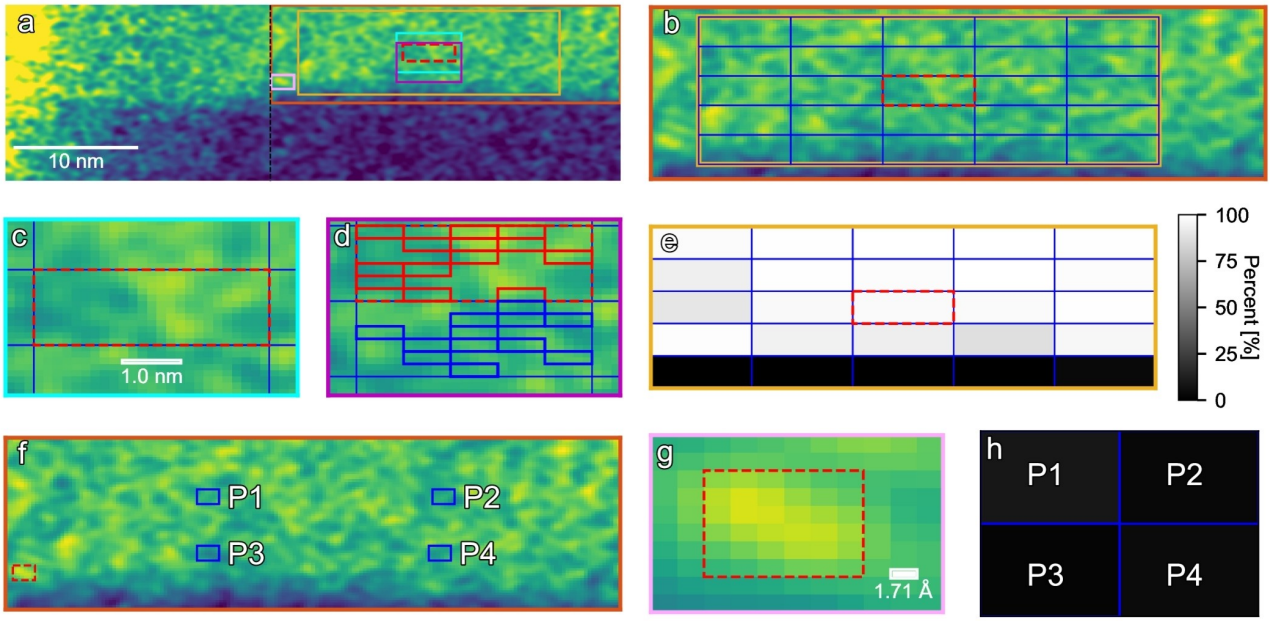

Figure 6. (a) Relative spectral contribution of the Sr EDX map obtained from the NMF broadened by a Gaussian filter to ease viewing. The colored rectangles show the positions of the following subplots: orange: b + f, cyan: c, magenta: d, pink: g. The dashed red rectangle is the reference area for the bulk Welch tests and the dashed line indicates the area where the sample has an even thickness (compare SI Figure S14). (b) Close up of the sample area with high Sr content. Random samples from the red dashed rectangle (close-up shown in (c)) are compared to random samples drawn from each individual blue rectangle in Welch tests. (d) One exemplary realization of random samples (smaller rectangles) drawn from each area (larger, confining rectangle) that are compared in a single Welch test. (e) Percentage of passed tests (see Table S2 in SI for exact numbers). (f) Location of passed one-sided Welch tests to test of higher Sr concentration (red dashed rectangle) close to the HAADF-determined surface with bulk position (blue rectangles). (g) Close-up of the area with higher Sr content. (h) Percentage of passed Welch tests, stating that the red area has a higher mean concentration than the blue areas specified in (f). The colormap is the same as used in (e).

regions improves the power of the test by yielding more normally distributed samples. True random sampling from the compared areas is important to enable a meaningful statistical evaluation.

A failure of the test indicates a high probability that the alternative hypothesis is true, with the significance of the test being reflected in the reproducibility of the results. We have here selected the settings such that the alternative hypothesis can be accepted with statistical relevance defined by a significance (P-value) lower than 0.05. A passed Welch test, on the other hand, can have two possible reasons: either the null hypothesis is really true or the chosen test settings are not able to resolve the desired property from the provided samples. It is thus only a weak indicator that the null hypothesis is true and other test settings and/or data are necessary to prove the hypothesis. Note that a hypothesis can never be proven directly, but indirect proof is possible by falsifying a suitable null hypothesis.

Even for a successful test, not all individual random Welch tests are necessarily delivering the same error-free results. As mentioned above, the reliability of the test is related to the significance, which indicates the smallest value level of α at which the null hypothesis can be rejected according to the provided samples. To further demonstrate the statistical robustness of the chosen test settings, 1000 Welch tests were performed for each comparison. The relative share of passed tests for the Sr bulk investigation is displayed in Figure 6e (see Table S2 in the SI for exact values). Within the bulk area itself (upper 20 regions), the majority of tests are passed (white color), indicating that the average mean between the areas is similar, or at least differences cannot be resolved with the chosen test settings. However, some of these regions on the left and lower edge show a higher failure rate, suggesting that there might be local changes in the areas themselves, which cannot be resolved with the chosen area size. The five lower areas fail the majority of the tests with significant accuracy (black color, compare Table S2), revealing a diverging mean Sr concentration in these areas compared to the central bulk reference region. Comparing the signal intensity in these areas with the reference, it becomes clear that these areas must contain less Sr, which is most probably due to the incipient complexion, for which we have shown before that it features much lower Sr concentrations than bulk LSM.[39]

This first analysis shows that nanoscale trends can be confirmed with Welch tests with significant certainty. However, small features like the oxide nucleation seeds found in the simulation require an even higher resolution. We thus compare one small region close to the complexion with potentially higher concentration to several bulk positions, in order to demonstrate the power of the conducted Welch test. Figure 6f gives an overview of the compared areas, with a close up of the reference area enclosed in red given in Figure 6f. With the new

hypothesis that the reference area has a higher concentration than the bulk areas, we can perform one-sided Welch test, which need less samples and do thus allow for a higher resolution. Note that, other than for the bulk Welch tests, here the random samples from compared areas are not re-binned, but the individual pixel values are taken. The area of such a random sample is thus only 1.95 Å^2. With an area containing only $6\times6=36$ of these, the resolution demonstrated here is 70.2 Å^2, which would correspond to a cluster containing only a few atoms in the xy dimensions.

As before, 1000 tests were performed. The percentage of passed tests is given in Figure 6h (see Table S3 in SI for numbers). The results of the tests suggest that the alternative hypothesis is accepted for all areas, stating that the mean concentration in the red area is significantly higher than in each of the ones marked in blue. These results demonstrate that the informative value of high resolution EDX measurements can be pushed to resolve concentrational deviations in areas down lower than the nanoscale. The selected combination of data post-processing methods demonstrated the resolution of minor changes in elemental distributions, and thus provides an indispensable tool for the detection of nucleation seeds. This now enables more detailed investigations of the complexion evolution over time and the linkage of concentration changes on its surface to cell deactivation.

The presented results render Sr segregation in SOCs a very probable reason for cell deactivation, in line with earlier findings at larger length scales. However, whether the segregated cations mainly lead to spatial blockage of the active site or to its loss via exsolution of the complexion, accompanied by the creation of voids and increasing porosity, needs yet to be determined at atomistic resolution. The proposed workflow provides a tool for an automated, robust, and fast analysis of EDX spectrum images necessary for such a detailed analysis of a large data stack, especially when the focus is on low-concentration elements such as strontium in the LSM perovskite studied here. This way, the cation agglomeration and nucleus growth can be tracked from early stages where only minute stoichiometric changes are anticipated. The flexible design of our routine based on multi-variate statistical analysis allows for easy and straightforward adaptation for the investigation of other materials. This is of high interest, especially for other electrode materials such as $La_xSr_{1-x}Co_yFe_{1-y}O_{3-\delta}$ (LSCF), for which high temperature environmental scanning electron microscopy spectra of the grain boundaries also hint at a Sr segregation pathway via a complexion.[80] However, further studies are needed to verify this conjecture and to establish the relevance of the proposed mechanism for other materials.

Surface Spectroscopy

In order to assess the potential enrichment of strontium at the surface, we have additionally conducted XPS measurements, as seen in Figure 7. In Figure 7a, the Sr 3d regions are plotted for two samples: one that has only been sintered at 1423 K for 1 h (pristine, blue), and one ('aged', orange) that has additionally been aged thermally at temperatures up to 1173 K for 150 without polarization. The left panel contains the surface-sensitive spectra that have been acquired with a kinetic energy of 130 eV, and the sub-surface-sensitive data is in the right panel (600 eV). According to the TPP-2M equation,[81] the escape depths for these kinetic energies can be estimated to be $3\lambda=$ 1.6 nm for the surface, and $3\lambda=4$ nm for sub-surface spectra (with λ being the inelastic mean free path). All spectra are normalized to the respective total La 3d area in order to investigate the distribution of A-site elements in the perovskite (when considering the form ABO_3). In the aged sample, there is a slight accumulation of strontium at the surface. More specifically, an increase of the Sr/La ratio of 11.5%, see also Table 1. This corresponds to an increase of 9.7% in the nominal A site occupancy by Sr, which might also result from segregation of strontium oxide. In addition, the sub-surface seems to be enriched in Sr in the aged sample, which could be explained by a diffusional concentration gradient originating from the LSM bulk.

The peak shapes of the Sr 3d surface and sub-surface spectra appear to be significantly different. Thus, peak fitting was performed, as shown in Figure 7b and Figure 7c. This procedure reveals that, in addition to the expected Sr 3d

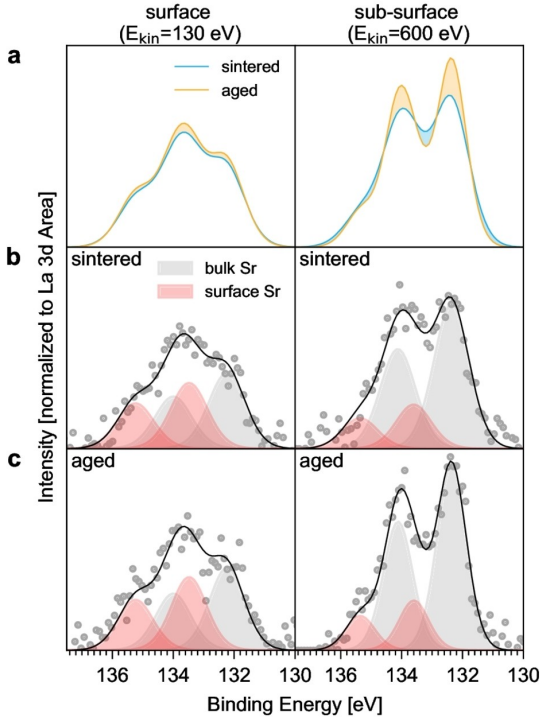

Figure 7. Sr 3d photoelectron spectra. (a) the surface (left) and sub-surface (right) spectra for the sintered and aged cells, normalized to the corresponding La 3d areas. During aging, the Sr/La ratio changes at the surface, see also Table 1. The blue and orange shaded regions illustrate regions where the sintered (blue) and aged (orange) spectra have higher intensities, respectively. In (b) and (c), peak fits of the Sr 3d region show that an additional component, shifted to higher binding energies compared to the bulk perovskite strontium, is present and seems to be accumulated at the surface, hence labeled as 'surface Sr'.

Table 1. The Sr/La ratio and fraction of Sr in the A site of the perovskite both increase upon thermal aging by 11.5% and 9.7%, respectively, while the fraction of surface Sr species ($Sr_{surf.}$) does not change significantly during the aging process.

condition	E_{kin} [eV]	Sr/La ratio	Sr in A site [at%]	$Sr_{surf.}$ [%]
sintered	130	0.169	14.5	46.5
sintered	600	0.212	17.5	23.4
aged	130	0.189	15.9	47.1
aged	600	0.224	18.3	21.1

doublet ($3d_{5/2}$ at a binding energy of 132.2 eV, colored gray in the plots), a second component is present in all spectra (red). This component is shifted to higher binding energies, with the $3d_{5/2}$ maximum at 133.6 eV and is more prominent in the surface spectra, where it makes up around 47% of the Sr 3d region for both samples, compared to just above 20% in the sub-surface. The main component thus seems to be the bulk oxide, which is in good agreement to literature values for perovskites,[82] and strontium oxide.[83]

The high-binding-energy component has been observed for other perovskites as well,[69] mostly being ascribed to carbonates.[83] Due to the generally very low amount of Sr in the sample (roughly 4 at% in LSM, accordingly less in the approximately 1:1 LSM/YSZ mixture), no distinct carbonate signal can be resolved in the C 1s spectra. Since it is thus not possible to clearly ascribe the component to a certain compound. We, thus, refer to it as'surface Sr', following the nomenclature recently used for lanthanum strontium ferrite.[69] In contrast to this system, the fraction of surface Sr species in LSM is, however, not increased after aging. Instead, the total amount of Sr is increased. As seen from Table 1, the fraction of bulk oxide species remains constant during aging. Thus, the observed Sr accumulation on the surface does not stem from the formation of secondary species, e.g. carbonate species, but from a general increase in Sr content towards the surface.

While it is impossible to draw the conclusion of where exactly the Sr agglomerations are located, i.e. at the complexion/vacuum interface or the LSM/vacuum interface, because XPS is a laterally integrative technique, the results seem to be in line with the simulation data in Figure 2. In order to further affirm this link, future experiments need to be performed on model systems with ultra-thin perovskite layers. That way, by means of synchrotron-based XPS depth profiling, the complexion can be probed directly and distinguished from the LSM/vacuum surface.

Conclusion

Combining MC and MD simulation, spatially resolved EDX-STEM mapping, and post-acquisition drift analysis, we could validate a predicted atomic scale Sr enrichment at the complexion/vacuum interface occurring on the LSM/YSZ side of SOECs after thermal aging up to 1073 K for 150 h. The results are complemented by surface-sensitive XPS measurements. In addition, simulations demonstrated increased diffusion rates in the complexion for both oxygen anions and cations, which has been corroborated by experimental observations. The formation of highly localized and atomically dispersed Sr enrichment at the complexion/vacuum interface which was found in the MC simulations could be validated by a newly developed, robust routine, which is based on STEM-EDX analysis, drift correction, NMF and Welch t-test. This automated data analysis is superior in spatial resolution and analysis times compared to standard evaluation procedures, while qualitatively similar results are obtained. This renders the outlined drift-corrected NMF analysis of large EDX stacks capable for high-throughput analysis to study the origins of compositional variations in SOECs down to the atomic scale. This will ultimately lead to improved structure-function correlations and a deepened understanding of deactivation processes.

Experimental and Methods Section

Theoretical methods

Monte Carlo Simulation

Two kinds of simulation cells were built and the preparational sintering process was simulated for 16 different doping realizations, each with the force-field based MC algorithm that has been described in previous work.[39] The cells that were obtained in this earlier work have been used to obtain ion diffusion coefficients across the interface using spatially restricted lag time mean square displacements.[48] For the surface simulations, a bigger cell containing a total of 21,330 atoms with lattice vectors measuring $22.4 \times 93.6 \times 147.9$ Å has been constructed in such a way, that a big hole cutting through the complexion between the two materials exposes two surfaces at the YSZ/LSM interface in the xz-plane (see SI Figure S1).

All cells have been aligned in the direction orthogonal to the complexion to match in the point of inflection of the fitted Mn elemental profiles across the complexion. Elemental profiles of MC-'sintered' cells with the described surface models were obtained from the projection of atom positions (up to ± 7 Å from the complexion center in z direction) overlaid with Gaussian functions to the y dimension. In order to include both surfaces featured in the cell, the elemental profiles were folded around the z direction at the middle of the simulation cell, which is 3 nm from either surface.

Molecular Dynamics

Molecular Dynamic simulations have been conducted for 1 ns after an equilibration time of 10 ps with a time step of 1 fs for 6 different structures employing LAMMPS.[84] The force field is the same as in the MC simulations. Spatial resolution of the diffusion is achieved by calculating the lag time mean square displacement for all atoms that have not left the region ± 5 Å around the specified point during the respective time periods.[48]

Sample preparation

The half cells, LSM||LSM+8YSZ||8YSZ, were prepared using yttria-stabilized zirconia (8YSZ, with 8 mol% Y_2O_3) electrolyte supports (Kerafol®, nominal diameter 20 mm and thickness

300 μm). Terpineol-based slurries were prepared with pure LSM ($(La_{0.8}Sr_{0.2})_{0.95}MnO_{3-\delta}$) powder (Fuel Cell Materials) and an LSM + YSZ (50/50) composite. First, an LSM + YSZ layer (thickness approximately 25 μm and diameter 8 mm) was symmetrically screen printed on both sides of the dense 8YSZ supports and after drying it at 353 K, an LSM layer (thickness about 25 μm, diameter 8 mm) was printed on both sides. The final sintering was performed at 1423 K for 1 h in air, with a heating rate of 2 $Kmin^{-1}$. One of the cells (labeled 'aged' throughout this manuscript) was further treated thermally for 150 h at temperatures of 1173 K in order to investigate the effects of thermal aging by means of EDX.

Specimens for electron microscopy were prepared by cutting the cells with a wire saw and subsequent polishing at an angle of 30°. From this oblique cross-section, a TEM lamella was prepared using an FEI Helios NanoLab G3 FIB-SEM Dualbeam system. Special care has been taken to avoid and remove re-deposited material at the interface of interest during the final low energy cleaning step.

For X-ray photoelectron spectroscopy (XPS) measurements, both cells (sintered and aged) were polished in plan-view, removing the LSM current collector layer (corresponding to the topmost 30 μm). Refer to Figure S2 for an optical microscopy image detailing one of these samples.

Electron microscopy and spectroscopy

STEM-EDX

TEM analysis – consisting of simultaneous image and EDX spectrum acquisition – was done in a ThermoFisher Scientific Talos F200X at 200 kV. The microscope was equipped with four silicon drift detectors (SDDs) in Super-X configuration, spanning a solid angle of 0.9 sr. A semi-convergence angle of 10.5 mrad was used with a beam current ranging between 50 to 450 pA. To improve the signal to noise ratio, multiple frames were acquired with the same parameters and summed up, applying an online drift correction based on cross correlation between each frame (Velox software, Thermo Fisher Scientific). Either raw data were used for further analysis, or background subtraction (empirical background model) was applied as well as prefiltering. For pre-filtering, the data were averaged over 4 (Figure 3) or 2 (Figure S3) next neighbor pixels, before EDX maps were extracted from the spectrum image data set. 4 pixels (Figure 3) relate to 3.5 nm and 2 pixels (Figure S3) relate to 328 pm. Pre-filtering reduces the spatial resolution. Note, the point resolution of the microscope is 160 pm. This is not the case for the data shown in Figure 5 (58 pm pixel size), in which the raw data (4D data stack, consisting of 175 frames, each including 3D spectrum image) is further analyzed.

Drift correction

While modern microscope acquisition software is equipped with real-time drift correction systems, there are cases where its performance is not sufficient, especially at high magnifications. Thus, we have developed an off-line, post-acquisition drift correction routine based on multiple template matching using scikit-image,[85] and subsequent outlier removal using random sample consensus (RANSAC).[78] In total, *N* templates (typically 100) are selected, with a few of them being placed manually and the rest of them randomly chosen. As shown in Figure S4, a region can be defined inside which all randomly assigned templates need to be located. Then, these templates are extracted from all image types acquired along with the SI spectrum image to make the procedure more robust to small changes in contrast (bright field images are especially prone to this). In our case, bright field (BF), dark field (DF) and high-angle annular dark field (HAADF) are obtained, thus increasing the number of available templates for the template matching by a factor of 3. These templates are matched for every frame in the spectrum image time series, after a Gaussian filter with $\sigma = 2$ px (corresponding to 0.639 nm) has been applied to both the templates and the images in order to avoid potential issues arising from the loss of atomic resolution due to focal changes. Instead of fitting a Euclidean transformation model to all 3*N* data, the robustness of the shift detection is improved by applying a RANSAC algorithm to the template match results, removing all outliers. By outsourcing the parameters to an external configuration file (in the YAML format), rapid screening of the optimal settings is possible in parallel. Afterwards, the drift correction is applied to the spectrum image stack.

Non-Negative Matrix Factorization

Each individual spatially resolved spectrum is convolved with a moving average with a window width of 100 eV. In order to increase the signal while still getting sufficient spatial resolution, spatial binning of the spectra with a bin size of 3 in x and 2 in y direction was performed. A Non-Negative Matrix Factorization (NMF) (employing the scikit-learn routine[86]) of the measured spectrum is used to identify the elemental composition at each measured spatial point. The initial component guess was based on experimental spectra originating from YSZ and LSM regions, far off the interface. Therefore, single element components (Y, Zr, La, Sr, Mn) were extracted from the experimental LSM and YSZ spectra using a home-made fitting routine, which combines serial and simultaneously Gauss peak fitting (Figure S5). These fitted components, together with a vector featuring the fitted background (Velox) and constructed spectra of other identified elements served as initial component guess.

Statistical Analysis

The mean concentrations at different areas with high resolution were investigated with Welch t-tests[79] performed on the elemental intensities obtained from the NMF. For two-sided Welch tests comparing solely the bulk regions, the 5.85 nm^2 areas were divided into 30 19.5 $Å^2$ sized samples, each containing 2×5 pixels of the maps obtained from NMF. The pixels in each sample are then aggregated into one value. 15 samples were drawn randomly with replacement from each investigated area. For the high resolution one-sided Welch tests, the investigated 70.2 $Å^2$ areas were divided into 36 of the 1.95 $Å^2$ NMF pixels and used directly in the test. 24 random samples were drawn from each area for each test. All tests were performed with a confidence interval of $\alpha = 0.95$ and without assumption of equal variances. Illustrations and further details on the execution of the tests are given in the respective results section.

X-ray photoelectron spectroscopy (XPS)

X-ray photoelectron spectra were acquired at the ISISS-PGM beam line at BESSY II for planpolished samples (see above). The setup consists of a Specs Phoibos 150 near-ambient pressure hemispherical sector analyzer and the measurements were performed in high vacuum at kinetic energies of 130 eV and 600 eV in order to achieve surface- and sub-surface-sensitivity. Spectral analysis was done in CasaXPS. Charge-induced drift was corrected for by using the C 1s region (adventitious carbon) and the valence band maximum. Shirley-type backgrounds were employed and for all fitted components, Pseudo-Voigt shapes with 30% Lorentzian character were used. For quantification, the peak areas were

corrected for the beamline flux (separately measured using a gold foil) and the respective cross sections.[87]

Acknowledgements

This work was supported by the Deutsche Forschungsgemeinschaft (DFG, German Research Foundation) under the priority programme SPP 2080 DynaKat. T. Götsch, F.-P. Schmidt, and T. Lunkenbein acknowledge support from the Federal Ministry of Education and Research in the framework of the project Catlab (03EW0015A). Moreover, this work was partially funded by the Deutsche Forschungsgemeinschaft (DFG, German Research Foundation) under Germany's Excellence Strategy – EXC 2089/1 – 390776260. The authors acknowledge the Helmholtz Zentrum Berlin für Materialien und Energie for allocating beam time within proposal number 221-10744CR. Additionally, the authors thank V. Vibhu for preparation of the electrodes. Open Access funding enabled and organized by Projekt DEAL.

Conflict of Interest

The authors declare no conflict of interest.

Data Availability Statement

The data that support the findings of this study are available from the corresponding author upon reasonable request.

Keywords: complexion · electron microscopy · interfaces · molecular modeling · segregation

[1] R. M. Ormerod, *Chem. Soc. Rev.* **2003**, *32*, 17–28.
[2] E. D. Wachsman, K. T. Lee, *Science* **2011**, *334*, 935–939.
[3] A. S. Brouwer, M. van den Broek, A. Seebregts, A. Faaij, *Renewable Sustainable Energy Rev.* **2014**, *33*, 443–466.
[4] S. R. Foit, I. C. Vinke, L. G. J. de Haart, R.-A. Eichel, *Angew. Chem. Int. Ed.* **2017**, *56*, 5402–5411; *Angew. Chem.* **2017**, *129*, 5488–5498.
[5] M. S. Sohal, J. E. O'Brien, C. M. Stoots, V. I. Sharma, B. Yildiz, A. Virkar, *J. Fuel Cell Sci. Tech.* **2012**, *9*, 011017.
[6] A. Atkinson, S. Barnett, R. J. Gorte, J. T. S. Irvine, A. J. McEvoy, M. Mogensen, S. C. Singhal, J. Vohs, *Nat. Mater.* **2004**, *3*, 17–27.
[7] S. He, S. P. Jiang, *Prog. Nat. Sci.* **2021**, *31*, 341–372.
[8] A. J. Jacobson, *Chem. Mater.* **2010**, *22*, 660.
[9] M. S. Khan, X. Xu, R. Knibbe, Z. Zhu, *Renewable Sustainable Energy Rev.* **2021**, *143*, 110918.
[10] A. Momma, T. Kato, Y. Kaga, S. Nagata, *J. Ceram. Soc. Jpn.* **1997**, *105*, 369–373.
[11] K. Chen, S. P. Jiang, *Int. J. Hydrogen Energy* **2011**, *36*, 10541–10549.
[12] S. N. Rashkeev, M. V. Glazoff, *Int. J. Hydrogen Energy* **2012**, *37*, 1280–1291.
[13] M. A. Laguna-Bercero, R. Campana, A. Larrea, J. A. Kilner, V. M. Orera, *J. Power Sources* **2011**, *196*, 8942–8947.
[14] J. A. Labrincha, J. R. Frade, F. M. Marques, *J. Mater. Sci.* **1993**, *28*, 3809.
[15] K. Yang, J. H. Shen, K. Y. Yang, I. M. Hung, K. Z. Fung, M. C. Wang, *J. Power Sources* **2006**, *159*, 63.
[16] Y. Huang, J. M. Vohs, R. J. Gorte, *J. Electrochem. Soc.* **2006**, *153*, A951.
[17] A. Chen, J. R. Smith, K. L. Duncan, R. T. DeHoff, K. S. Jones, E. D. Wachsman, *J. Electrochem. Soc.* **2010**, *157*, B1624.
[18] M. Keane, M. K. Mahapatra, A. Verma, P. Singh, *Int. J. Hydrogen Energy* **2012**, *37*, 16776–16785.
[19] K. Chen, S. P. Jiang, *J. Electrochem. Soc.* **2016**, *163*, F3070–F3083.
[20] J. Kim, H. I. Ji, H. P. Dasari, D. Shin, H. Song, J. H. Lee, B. K. Kim, H. J. Je, H. W. Lee, K. J. Yoon, *Int. J. Hydrogen Energy* **2013**, *38*, 1225–1235.
[21] H. Kumigashira, K. Horiba, H. Ohguchi, K. Ono, M. Oshima, N. Nakagawa, M. Lippmaa, M. Kawasaki, H. Koinuma, *Appl. Phys. Lett.* **2003**, *82*, 3430–3432.
[22] K. Katsiev, B. Yildiz, K. Balasubramaniam, P. A. Salvador, *Appl. Phys. Lett.* **2009**, *95*, 4–7.
[23] A. K. Huber, M. Falk, M. Rohnke, B. Luerssen, M. Amati, L. Gregoratti, D. Hesse, J. Janek, *J. Catal.* **2012**, *294*, 79–88.
[24] W. Lee, J. W. Han, Y. Chen, Z. Cai, B. Yildiz, *J. Am. Chem. Soc.* **2013**, *135*, 7909–7925.
[25] S. P. Jiang, J. G. Love, *Solid State Ion.* **2001**, *138*, 183–190.
[26] N. Caillol, M. Pijolat, E. Siebert, *Appl. Surf. Sci.* **2007**, *253*, 4641–4648.
[27] X. Yang, J. Hardy, C. A. Coyle, J. F. Bonnett, S. M. Mahserejian, J. W. Stevenson, *J. Electrochem. Soc.* **2022**, *169*, 024512.
[28] H. P. Buchkremer, U. Dieckmann, D. Stöver, in *Second European Solid Oxide Fuel Cell Forum*, Proceedings Vol. 1 (Ed.: Ulf Bossel), Oslo, **1996**, p. 221.
[29] V. A. Haanappel, J. Mertens, D. Rutenbeck, C. Tropartz, W. Herzhof, D. Sebold, F. Tietz, *J. Power Sources* **2005**, *141*, 216–226.
[30] S. P. Jiang, *J. Mater. Sci.* **2008**, *43*, 6799–6833.
[31] G. Chen, Y. Gao, Y. Luo, R. Guo, *Ceram. Int.* **2017**, *43*, 1304–1309.
[32] J. Liu, Y. Yu, T. Yang, O. Ozmen, H. Finklea, E. M. Sabolsky, H. Abernathy, P. R. Ohodnicki, G. A. Hackett, *ECS Trans.* **2017**, *78*, 689.
[33] Y. Song, X. Zhang, Y. Zhou, Q. Jiang, F. Guan, H. Lv, G. Wang, X. Bao, *Energy Storage Mater.* **2018**, *13*, 207–214.
[34] T. Wu, W. Zhang, Y. Li, Y. Zheng, B. Yu, J. Chen, X. Sun, *Adv. Energy Mater.* **2018**, *8*, 1–7.
[35] M. S. Khan, X. Xu, J. Zhao, R. Knibbe, Z. Zhu, *J. Power Sources* **2017**, *359*, 104–110.
[36] Y. Wang, W. Li, L. Ma, W. Li, X. Liu, *J. Mater. Sci. Technol.* **2020**, *55*, 35–55.
[37] B. Koo, K. Kim, J. K. Kim, H. Kwon, J. W. Han, W. C. Jung, *Joule* **2018**, *2*, 1476–1499.
[38] K. Chen, S. P. Jiang, *Electrochem. Energy Rev.* **2020**, *3*, 730–765.
[39] H. Türk, F.-P. Schmidt, T. Götsch, F. Girgsdies, A. Hammud, D. Ivanov, I. C. Vinke, L. De Haart, R.-A. Eichel, K. Reuter, R. Schlögl, A. Knop-Gericke, C. Scheurer, T. Lunkenbein, *Adv. Mater. Interfaces* **2021**, *8*, 2100967.
[40] T. Götsch, H. Türk, F.-P. Schmidt, I. C. Vinke, L. De Haart, R. Schlögl, K. Reuter, R.-A. Eichel, A. Knop-Gericke, C. Scheurer, T. Lunkenbein, *ECS Trans.* **2021**, *103*, 1331–1337.
[41] S. J. Dillon, M. Tang, W. C. Carter, M. P. Harmer, *Acta Mater.* **2007**, *55*, 6208–6218.
[42] P. R. Cantwell, M. Tang, S. J. Dillon, J. Luo, G. S. Rohrer, M. P. Harmer, *Acta Mater.* **2014**, *62*, 1–48.
[43] A. Kundu, K. M. Asl, J. Luo, M. P. Harmer, *Scr. Mater.* **2013**, *68*, 146–149.
[44] A. R. Krause, P. R. Cantwell, C. J. Marvel, C. Compson, J. M. Rickman, M. P. Harmer, *J. Am. Ceram. Soc.* **2018**, *102*, 778–800.
[45] P. Xu, W. Rheinheimer, S. N. Shuvo, Z. Qi, O. Levit, H. Wang, Y. Ein-Eli, L. A. Stanciu, *ChemElectroChem* **2019**, *6*, 4576–4585.
[46] J. Luo, *Energy Storage Mater.* **2019**, *21*, 50–60.
[47] J. Timmermann, F. Kraushofer, N. Resch, P. Li, Y. Wang, Z. Mao, M. Riva, Y. Lee, C. Staacke, M. Schmid, C. Scheurer, G. S. Parkinson, U. Diebold, K. Reuter, *Phys. Rev. Lett.* **2020**, *125*, 206101.
[48] S. Stegmaier, R. Schierholz, I. Povstugar, J. Barthel, S. P. Rittmeyer, S. Yu, S. Wengert, S. Rostami, H. Kungl, K. Reuter, R. A. Eichel, C. Scheurer, *Adv. Energy Mater.* **2021**, *11*, 2100707.
[49] L. Masliuk, F.-P. Schmidt, W. Hetaba, M. Plodinec, G. Auffermann, K. Hermann, D. Teschner, F. Girgsdies, A. Trunschke, R. Schlögl, T. Lunkenbein, *J. Phys. Chem. C* **2020**, *124*, 23069–23077.
[50] K. Reuter, *Catal. Lett.* **2016**, *146*, 541–563.
[51] P. Potapov, A. Lubk, *Micron* **2021**, *145*, 103068.
[52] N. Braidy, R. Gosselin, *Sci. Rep.* **2019**, *9*, 18797.
[53] S. Cacovich, F. Matteocci, M. Abdi-Jalebi, S. D. Stranks, A. Di Carlo, C. Ducati, G. Divitini, *ACS Appl. Energ. Mater.* **2018**, *1*, 7174–7181.
[54] P. Potapov, P. Longo, E. Okunishi, *Micron* **2017**, *96*, 29–37.
[55] J. Titchmarsh, *Micron* **1999**, *30*, 159–171.
[56] J. Titchmarsh, S. Dumbill, *J. Microsc.* **1996**, *184*, 195–207.
[57] M. Shiga, K. Tatsumi, S. Muto, K. Tsuda, Y. Yamamoto, T. Mori, T. Tanji, *Ultramicroscopy* **2016**, *170*, 43–59.
[58] B. R. Jany, A. Janas, F. Krok, *Nano Lett.* **2017**, *17*, 6520–6525.

[59] N. H. Timm, in *Applied Multivariate Analysis*, Springer-Verlag New York, **2004**.
[60] W. K. Härdle, L. Simar, in *Applied Multivariate Statistical Analysis*, 3rd ed., Springer-Verlag Berlin Heidelberg, **2012**.
[61] K. Devarajan, *PLoS Comput. Biol.* **2008**, *4*, e1000029.
[62] A. R. McIntosh, B. Mišić, *Annu. Rev. Psychol.* **2013**, *64*, 499–525.
[63] M. Chang, in *Modern Issues and Methods in Biostatistics*, Springer Science + Business Media, **2019**.
[64] P. Potapov, P. Longo, E. Okunishi, *Micron* **2017**, *96*, 29–37.
[65] P. Potapov, A. Lubk, *Adv. Struct. Chem. Imaging* **2019**, *5*, 4.
[66] G. Lucas, P. Burdet, M. Cantoni, C. Hébert, *Micron* **2013**, *52–53*, 49–56.
[67] N. Dobigeon, N. Brun, *Ultramicroscopy* **2012**, *120*, 25–34.
[68] P. Cao, P. Tang, M. F. Bekheet, H. Du, L. Yang, L. Haug, A. Gili, B. Bischoff, A. Gurlo, M. Kunz, R. E. Dunin-Borkowski, S. Penner, M. Heggen, *J. Phys. Chem. C* **2022**, *126*, 786–796.
[69] Đ. Tripković, J. Wang, R. Küngas, M. B. Mogensen, B. Yildiz, P. V. Hendriksen, *Chem. Mater.* **2022**, *34*, 1722–1736.
[70] J. M. Polfus, B. Yildiz, H. L. Tuller, *Phys. Chem. Chem. Phys.* **2018**, *20*, 19142–19150.
[71] M. P. De Jong, I. Bergenti, V. A. Dediu, M. Fahlman, M. Marsi, C. Taliani, *Phys. Rev. B* **2005**, *71*, 2–5.
[72] M. Backhaus-Ricoult, K. Adib, T. St. Clair, B. Luerssen, L. Gregoratti, A. Barinov, *Solid State Ion.* **2008**, *179*, 891–895.
[73] M. Rohnke, K. Schaepe, A. K. Bachmann, M. Laenger, J. Janek, *Appl. Surf. Sci.* **2017**, *422*, 817–827.
[74] Q. H. Wu, M. Liu, W. Jaegermann, *Mater. Lett.* **2005**, *59*, 1980–1983.
[75] T. T. Fister, D. D. Fong, J. A. Eastman, P. M. Baldo, M. J. Highland, P. H. Fuoss, K. R. Balasubramaniam, J. C. Meador, P. A. Salvador, *Appl. Phys. Lett.* **2008**, *93*, 1–4.
[76] D. Kim, R. Bliem, F. Hess, J. J. Gallet, B. Yildiz, *J. Am. Chem. Soc.* **2020**, *142*, 3548–3563.
[77] F. Hess, B. Yildiz, *J. Chem. Phys.* **2021**, *154*, 064702.
[78] M. A. Fischler, R. C. Bolles, *Commun. ACM* **1981**, *24*, 381–395.
[79] J. Hedderich, L. Sachs, *Angewandte Statistik*, 16th ed., Springer-Verlag GmbH Deutschland, **2018**, pp. 445–470.
[80] M. A. Niania, R. Podor, T. B. Britton, S. J. Skinner, J. A. Kilner, *Microsc. Microanal.* **2016**, *22*, 10–11.
[81] S. Tanuma, C. J. Powell, D. R. Penn, *Surf. Interface Anal.* **2003**, *35*, 268–275.
[82] R. Vasquez, *J. Electron Spectrosc. Relat. Phenom.* **1991**, *56*, 217–240.
[83] M. I. Sosulnikov, Y. A. Teterin, *Doklady AN SSSR* **1991**, *317*, 418.
[84] S. Plimpton, *J. Comput. Phys.* **1995**, *117*, 1–19.
[85] S. van der Walt, J. L. Schönberger, J. Nunez-Iglesias, F. Boulogne, J. D. Warner, N. Yager, E. Gouillart, T. Yu, *PeerJ* **2014**, *2*, e453.
[86] F. Pedregosa, G. Varoquaux, A. Gramfort, V. Michel, B. Thirion, O. Grisel, M. Blondel, P. Prettenhofer, R. Weiss, V. Dubourg, J. Vanderplas, A. Passos, D. Cournapeau, M. Brucher, M. Perrot, E. Duchesnay, *J. Mach. Learn. Res.* **2011**, *12*, 2825–2830.
[87] J. J. Yeh, I. Lindau, *At. Data Nucl. Data Tables* **1985**, *32*, 1–155.

Manuscript received: March 1, 2022
Revised manuscript received: July 5, 2022
Accepted manuscript online: July 8, 2022
Version of record online: August 1, 2022